Unclad Microphotonics for Terahertz Waveguides and Systems

Daniel Headland, Withawat Withayachumnankul, *Senior Member, IEEE*, Xiongbin Yu, Masayuki Fujita, *Member, IEEE*, and Tadao Nagatsuma, *Fellow, IEEE*

***Abstract*—A practical approach to realize substrateless, unclad, micro-scale intrinsic silicon waveguides for the terahertz range is presented. The waveguides are monolithically integrated within a supporting silicon frame, with which they are fabricated together from the same silicon wafer in a single-mask etching process. This establishes an integration platform to house many diverse components and facilitates packaging. Effective medium techniques are deployed to prevent the frame from interfering with the waveguide's functionality. Straight waveguides of this sort are experimentally found to be efficient and broadband. Elementary components including Y-junctions and evanescent couplers are developed, and deployed in demonstrations of applications for terahertz waves including sensing and communications. This is a promising pathway to realize future microphotonic devices for diverse applications of terahertz waves.**

***Index Terms*—Terahertz, waveguide, photonics, silicon, communications, sensing.**

I. Introduction

THE development of practical terahertz systems is strongly dependent upon the availability of a rigid waveguiding platform, to support integration, compactness, and packaging. Physically machined hollow metallic waveguides are currently dominant in this regard, and are a commercially-available product that is commonplace in terahertz laboratories [1], [2]. Such waveguides may also be fabricated by coating 3D-printed plastic structures with metal [3], [4], or by stacking a series of metal-coated semiconductor wafers that are etched with micro-scale trenches [5]–[8]. However, all of these fabrication techniques are reasonably complex, as it is fundamentally challenging to realize an internally-smooth micro-scale hollow channel that is enclosed by metal on all sides. As such, hollow metallic waveguides are unsuited to high-volume manufacture. Furthermore, metals suffer from increasing Drude loss at high frequencies [9], which negatively impacts overall efficiency. These limitations motivate investigations into all-silicon structures for terahertz waveguiding, as high-resistivity float-zone intrinsic silicon is a near-lossless dielectric in the terahertz range. Furthermore, the refractive index of silicon is sufficiently high to achieve strong field confinement.

All-dielectric terahertz waveguides have been realized in a silicon-on-insulator platform, in which high-index micro-scale silicon waveguides rest upon a supporting dielectric substrate [10], [11]. The substrate is frequently more absorptive than intrinsic silicon, but losses in the substrate can be lessened by excavating a portion of dielectric beneath the waveguide, to realize suspended waveguides [12]–[14]. Micro-scale silicon waveguides can also be made entirely substrateless, which reduces fabrication complexity, and avoids dielectric absorption in the substrate altogether. For such substrateless silicon devices, physical support for the waveguide channel must be provided by in-plane structures that are etched from the same silicon wafer, which should be engineered to minimize leakage loss. This is commonly achieved using a two-dimensional photonic crystal that is implemented with a periodic through-hole array in the silicon slab [15]–[21]. For such photonic crystal waveguides, in-plane field confinement is achieved using the photonic bandgap effect that is provided by photonic crystals, and out-of-plane confinement is provided by total internal reflection. One disadvantage of photonic crystal waveguides is that bandwidth and dispersion performance is typically limited, thereby reducing their applicability to wideband applications such as terahertz communications. Furthermore, it is not trivial to implement elementary passive components such as bends and splitters with a photonic crystal waveguide. For these reasons, recent years have seen the photonic crystal replaced with effective medium, in order to lower the effective index of the silicon that surrounds the waveguide, and achieve in-plane field confinement using the broadband phenomenon of total internal reflection, rather than a photonic bandgap [22]. As with photonic crystal, the effective medium is implemented using a periodic through-hole array,

Manuscript received April 28, 2020; revised August 17, 2020; accepted September 1, 2020. Date of publication September 4, 2020; date of current version December 15, 2020. The work was supported in part by the Core Research for Evolutional Science and Technology (CREST) Program, in part by the Japan Science and Technology Agency (JST) under Grant JPMJCR1534, in part by the Grant-in-Aid for Scientific Research, in part by the Ministry of Education, Culture, Sports, Science and Technology of Japan under Grant 20H01064, and in part by Discovery Project, The Australian Research Council (Project No. ARC DP180103561). *(Corresponding author: Daniel Headland.)*

Daniel Headland, Masayuki Fujita, and Tadao Nagatsuma are with Information Photonics Group, Graduate School of Engineering Science, Osaka University, Toyonaka 560-8531, Japan (e-mail: headland@ee.es.osaka-u.ac.jp; fujita@ee.es.osaka-u.ac.jp; nagatuma@ee.es.osaka-u.ac.jp).

Withawat Withayachumnankul is with Terahertz Engineering Laboratory, School of Electrical and Electronic Engineering, The University of Adelaide, Adelaide, SA 5005, Australia (e-mail: withawat@adelaide.edu.au).

Xiongbin Yu was with Osaka University, Osaka 565-0871, Japan. He is currently with the Laboratory for Future Interdisciplinary Research of Science, and Technology, Institute of Innovative Research, Tokyo Institute of Technology, Tokyo 152-8550, Japan (e-mail: yu.x.ad@m.titech.ac.jp).

This article has supplementary downloadable material available at https://ieeexplore.ieee.org, provided by the authors.

Color versions of one or more of the figures in this article are available online at https://ieeexplore.ieee.org.

Digital Object Identifier 10.1109/JLT.2020.3021681

albeit of smaller hole pitch and size. This approach yields a substrateless all-silicon terahertz waveguide that exhibits broad bandwidth and highly efficient propagation, at the cost of reduced in-plane confinement.

A periodic through-hole array is an intricate microstructure that requires careful design and accurate fabrication in order to serve as support for a substrateless all-silicon terahertz waveguide. These stringent requirements motivate the removal of in-plane cladding structures, to facilitate greater control over physical parameters such as waveguide thickness, bend curvature, and structure—without potentially adverse effects arising from disturbing the regularity of the through-hole array that comprises the cladding. It would also engender simplicity; there are fewer intricate micro-scale features overall, leading to more-rapid simulation and design, and a lower probability of negative impacts of non-ideal fabrication quality. In this work, we present a practical approach to achieve all-silicon terahertz photonic waveguides that are both substrateless and unclad, by monolithic integration with a silicon frame structure at the boundary of the terahertz photonic circuit. This frame is physically robust, but serves no electromagnetic purpose, and effective medium is employed to electromagnetically separate the frame from the waveguide. Thus, the frame can readily be employed to handle, secure, and package the patterned silicon samples without interfering with the functionality of the terahertz photonic circuit. This approach is distinguished from previously demonstrated unclad all-silicon waveguides [23]–[25] in that the waveguides in this work only make contact with the frame at the edge of the circuit, rather than with periodic silicon tethers that affix the waveguide to adjacent supporting structures on both sides. As a result, the central area that is surrounded by the frame can be made electrically large in both dimensions, in order to accommodate diverse terahertz photonic circuits.

In addition to waveguides, we develop key passive photonic components, and deploy them in practical applications of terahertz waves, i.e. communications and sensing, which are rendered feasible by the supporting frame. Using this unclad microphotonic platform, several integrated passive terahertz components could straightforwardly be interconnected within a single frame. This would realize complex and sophisticated passive systems, which are all defined with a single mask, and etched simultaneously together from a high-resistivity float-zone intrinsic silicon wafer—engendering high efficiency. This is therefore a promising candidate for a general-purpose integration platform for terahertz waves.

II. All-Silicon Terahertz Platform

The central concept of this work is illustrated in Fig. 1(a). A silicon waveguide and supporting frame are etched together from an intrinsic silicon wafer. The point at which the waveguide is attached to the frame is perforated with a dense hole lattice, in order to realize an effective medium of low effective index. As such, terahertz waves that are confined within the waveguide undergo total internal reflection when they are incident upon this effective medium, and remain within the waveguide itself. Thus, the effective medium exhibits electromagnetic functionality that is as similar as possible to free space, but in structural terms, it provides essential physical support. The separation between the waveguide and the unpatterned portions of the supporting frame is sufficiently large so as to avoid interaction, for which a distance of approximately two free-space wavelengths is deemed sufficient, as a conservative estimate. External to the frame,

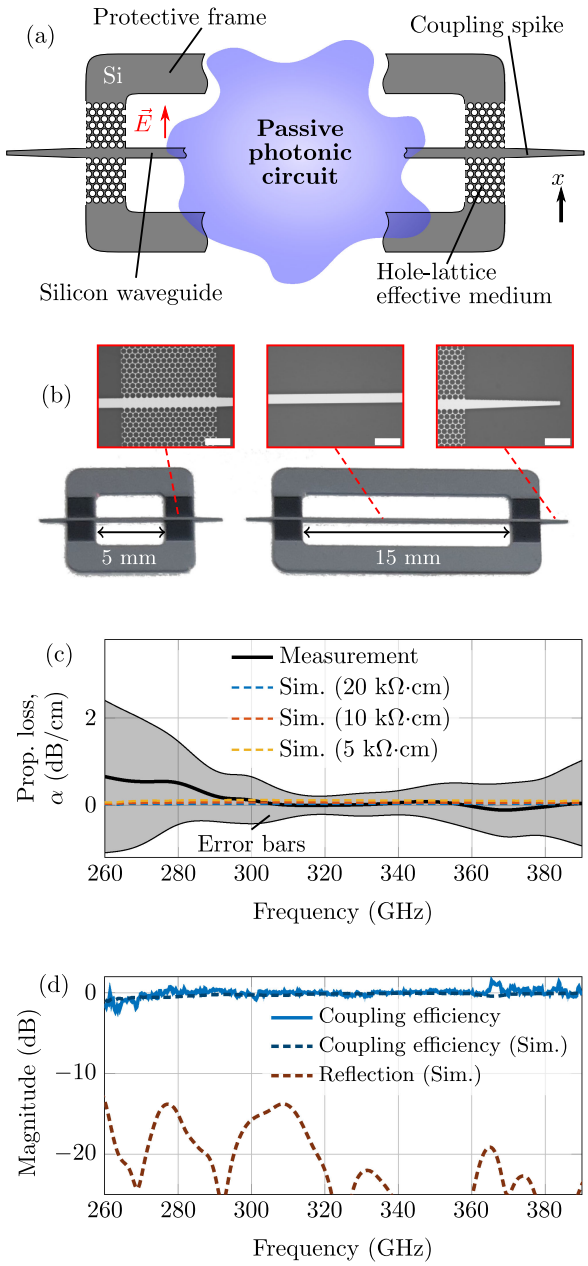

Fig. 1. The unclad microphotonics concept, (a) an illustration showing silicon supporting frame and effective medium cladding at the waveguide's attach point, as well as the in-plane polarization employed in this work, (b) straight waveguides of width 200 µm, frame-width 2 mm, and lateral separation of 2 mm between the waveguide and frame. as well as inset micrographs with 500 µm scale bars, showing equilateral triangular through-hole lattice with pitch 120 µm and diameter 110 µm, (c) measured propagation loss of the waveguides shown in (b), with a single standard deviation-span given as a gray area, as compared to simulation, and (d) coupling efficiency and reflection of a single port, when excited from a hollow metallic waveguide into which the coupling spike is inserted.

the silicon waveguide is progressively tapered so as to provide broadband index matching, thereby yielding an interface to the outside world, and suppressing reflections and standing waves. Within the frame, the arrangement of the terahertz photonic circuit itself is near-arbitrary, with the sole constraint being that all features must have sufficient structural support, as well as distance from the unpatterned portions of the frame. If an isolated silicon feature is desired, such as an evanescently-coupled resonator, then effective medium may be employed to provide a physical bridge to the remainder of the circuit, whilst avoiding a direct photonic connection to a silicon waveguide.

In the context of this work, some basic physical parameters are fixed in order to maintain a manageable scope for a single study. Silicon thickness is 200 μm, frame width is 2 mm, waveguide width is 200 μm, and all coupling spikes are 2 mm-long linear tapers that terminate in a 80 μm-wide snub. The effective medium at the attach point is implemented using an equilateral triangular hole lattice of cylindrical through-holes with pitch 120 μm and hole diameter 110 μm. It is noted that these lattice parameters are very closely related to that of the effective medium-clad terahertz waveguides that are presented in [22]. Indeed, the portion of the waveguide that passes through the frame could be viewed as a length of effective-medium-clad waveguide of the same sort that is described in the cited work. Aside from physical parameters, the mode that is utilized by all devices presented in this study is also fixed; the E_{11}^{x}, in-plane-polarized mode is employed, as indicated in Fig. 1(a). It is noted that there is no special significance to this particular choice, as the unclad waveguide is also capable of supporting the out-of-plane polarization, i.e. normal to the surface of the silicon wafer. A brief analysis of the number and effective model index of propagating modes is performed using a variant of Marcatili's method [26], and results are given in the Supporting Information that accompanies this article. It is found that higher-order modes do not propagate for frequencies below 363 GHz, and are leaky for frequencies below ∼388 GHz. For the dominant E_{11}^{x} mode, the field confinement factor [27], i.e. the proportion of the mode's energy flux density within the dielectric volume, is 61%, 88%, and 92% at 275 GHz, 325 GHz, and 375 GHz, respectively.

A. Straight Waveguides

The most fundamental component of a passive photonic circuit is a straight dielectric waveguide. Different lengths of straight waveguide are devised, where each is housed within a dedicated frame, and fabricated from high-resistivity float-zone intrinsic silicon wafers of nominal resistivity >10 kΩ·cm using deep-reactive ion etching (DRIE). The resulting devices are shown in Fig. 1(b), with micrographs of key salient features of electromagnetic significance. The power transmission through these straight waveguides is probed by inserting both coupling spikes into hollow metallic waveguides, following the example of [17]. In this case, the hollow waveguides are of rectangular inner dimensions 711 μm × 356 μm, targeting the 260 GHz–400 GHz band. Alignment between the silicon spike and metal waveguide is performed using manual actuation with accurate micrometer stages. The hollow waveguides serve as an interface to a high-quality, commercially-available all-electronic measurement system, in which the output of a mm-wave signal generator is applied to a ×9 frequency multiplier, producing terahertz waves in the range from 260 GHz to 390 GHz. At the detector side, frequency down-conversion is performed using a terahertz mixer circuit, producing microwave signals that may be processed by a spectrum analyzer, yielding accurate terahertz transmission magnitude data. As imperfect alignment between the silicon and hollow waveguide is a cause of coupling loss, optimal alignment is sought by progressive adjustment of the micrometer stages, whilst visually monitoring the trace that is displayed on the spectrum analyzer. Several 5 mm and 15 mm-long waveguides are probed in this way, and the difference in power transmission between the two is employed to estimate the propagation loss, α, of the straight waveguide. Numerous measurements are taken for each waveguide length, resulting in several pairs of measurements with different-length samples. For each such pair, the difference in transmission is extracted, and divided by the disparity in distance, to compute a single frequency-dependent propagation-loss profile. The mean and standard deviation of these profiles is employed to construct error-bars. Owing to the low absorption of high-resistivity intrinsic silicon, the variation due to minor discrepancies in manual alignment is more significant than the propagation loss itself. For this reason, both mean and standard deviation are smoothed in post-processing [28], in order to extract an overall trend, and the results are given in Fig. 1(c).

In order to compare measured propagation loss to expectation, simulations are performed in which a Drude model is employed to account for dielectric absorption and material dispersion of intrinsic silicon. Several different lengths of waveguide are simulated, with the frame omitted, and the expected propagation loss is extracted by comparison of transmission magnitude. As the specific value of resistivity is not explicitly known, a range is simulated, and results are shown in Fig. 1(c). According to these results, propagation loss across the measurable bandwidth is less than 0.117 dB/cm for 5 kΩ·cm, less than 0.059 dB/cm for 10 kΩ·cm, and less than 0.032 dB/cm for 20 kΩ·cm. Thus, simulated propagation loss is situated within the bounds of the smoothed error bars of the measured propagation loss, for all values of resistivity employed. We may conclude that simulation and experiment are in approximate agreement, that this is indeed a low-loss waveguide, and that this remains true for a range of material resistivity.

The influence of the coupling structure and the point at which the waveguide makes contact with the supporting frame is of interest. This is because it determines coupling efficiency, which is of key importance to the overall performance of passive circuits that are founded upon this platform. Transmission through the straight silicon waveguides shown in Fig. 1(b) is normalized by a back-to-back measurement, in which the hollow metallic waveguides of the source and detector are coupled directly together (not shown). The influence of propagation loss is removed, and the resulting decibel value is divided by two in order to approximate the coupling efficiency of a single port. The results are shown in Fig. 1(d), where it can be seen that close agreement with simulation is attained, and that the −3 dB bandwidth boundary

is not encountered across the measurable range of frequencies. Points at which measured coupling efficiency exceeds 0 dB, e.g. in the vicinity of 365 GHz, are understood as the result of imperfect alignment in the reference measurement. It is noted that, owing to the low absorption of intrinsic silicon, this material is approximated as a lossless dielectric of relative permittivity $\epsilon = 11.68$ in these simulations, and in all subsequent simulation results that are presented in this article, for simplicity. Aside from coupling efficiency, the reflection from the coupling structure is also of interest, but this may only be investigated in simulation due to limitations in the available experimental equipment. A simulation is devised in which all energy that is coupled to the unclad waveguide is simply absorbed, in order to remove the influence of subsequent reflections from other features. The results of this simulation are shown in Fig. 1(d), where it can be seen that reflection magnitude is below -13 dB across the measurable bandwidth.

B. Structural Robustness and Versatility

The degree of design freedom that is afforded by the proposed terahertz microphotonic platform is of interest. Specifically, it is desirable to know whether the silicon micro-beams that comprise the waveguides can be made longer and thinner, and remain structurally self-supporting. Thus, a sample is devised that exhibits no useful electromagnetic functionality, but rather, its sole purpose is to provide insight into robustness. Several silicon micro-beams are housed together within a single supporting frame, of width ranging from 200 µm to 10 µm—around a hundredth of a free-space wavelength—and coupling spikes are omitted, as shown in Fig. 2(a). The photograph given in Fig. 2(b) shows that the total silicon micro-beam length is 3 cm. The two largest silicon micro-beam widths are 150 µm and 200 µm, and for two of each, a gap is introduced into the micro-beam, and hence there is only a single attach point to the supporting frame. The sample has proven to be sufficiently robust to survive transport (i.e. from the foundry) and manual handling with ordinary tweezers. Furthermore, the gaps show that only a single attach-point is required to support the long silicon micro-beams. This sample therefore gives an indication of the significant design freedom that is offered by unclad microphotonics. It is also noted that, although 10 µm is the minimum width employed in this work, narrower beams may be viable. A definitive answer to this question would require a separate study that is dedicated to the physical robustness of single-crystal silicon microbeams.

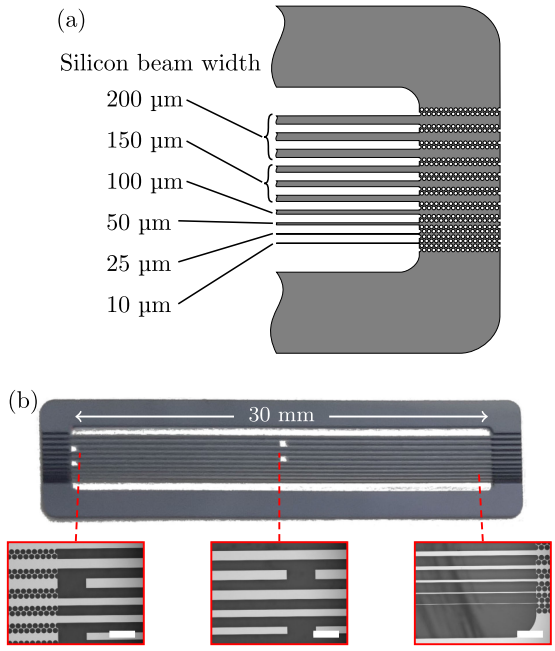

Fig. 2. A silicon sample that bears an array of silicon micro-beams, of width ranging from 10 µm to 200 µm, showing (a) schematic of the right side of the sample, and (b) photograph of the whole sample, where two 150 µm micro-beams and two 200 µm micro-beams have gaps, and hence are attached to the frame at only one point. Micrographs are included, for which all scale bars are 500 µm.

III. Y-Junction

A. Design and Characterization

Having demonstrated straight waveguides in Section II-A, it is appropriate to develop useful elementary passive components. We will begin with a Y-junction, which can serve as both a splitter and combiner of terahertz waves. This component is implemented with a symmetrically-reflected 90° circular bend, of radius 2 mm. Analysis of the loss of a waveguide bend in isolation is presented in the Supporting Information that accompanies this article. The Y-junction is housed within a supporting frame, and fabricated using DRIE. The resulting sample is shown in Fig. 3(a),(b). The power transmission between specific port-pairs is probed by inserting the relevant coupling spikes into hollow metallic waveguides that are coupled to terahertz sources and detectors, as shown in Fig. 3(c),(d). The electronic measurement system is identical to that which is described in Section II-A. The measured value is normalized by the response of a straight waveguide, in order to isolate the the magnitude of the S-parameters of the Y-junction itself, and deembed them from the coupling structure and measurement system. The results are given in Fig. 3, showing close agreement with the results of full-wave simulations. For $S_{21} = S_{31}$, the loss that is in excess of the -3 dB that is expected from even power splitting is in the vicinity of -0.5 dB for frequencies above 280 GHz, corresponding to 90% efficiency. As the absorption of the intrinsic silicon is essentially negligible, the loss is chiefly due to radiation at the center of the junction. It is also noted that $S_{12} = S_{21}$, and $S_{13} = S_{31}$, due to reciprocity. Significant transmission between Port 3 and Port 2 is undesired, and although it is non-negligible, it is below ~ -10 dB across the measurable bandwidth. A null is noted at 360 GHz, and is ascribed to cancellation between the power that is conveyed from Port 2 to Port 3 directly across the Y-junction, and that which enters the stem of the Y-junction and is reflected from Port 1. The frequency of this null differs slightly from simulation, as there is no metal waveguide attached to Port 1 in the measurement.

The simulated reflection response of the Y-junction is included in the Supporting Information. For all ports, peak reflection is ~ -7 dB, in the vicinity of $\sim$310 GHz. As this is greater than the reflection response that is observed in Fig. 1(d), we may

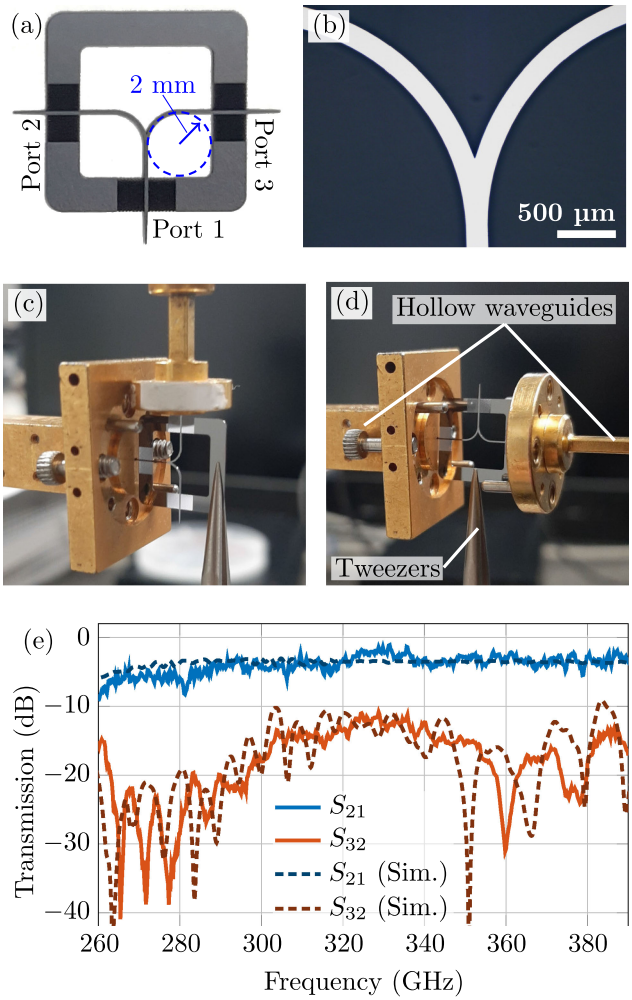

Fig. 3. A Y-junction, showing (a) an annotated photograph and (b) a micrograph of the device, (c),(d) experimental characterization, of S_{21} and S_{32}, respectively, and (e) measured and simulated S-parameters.

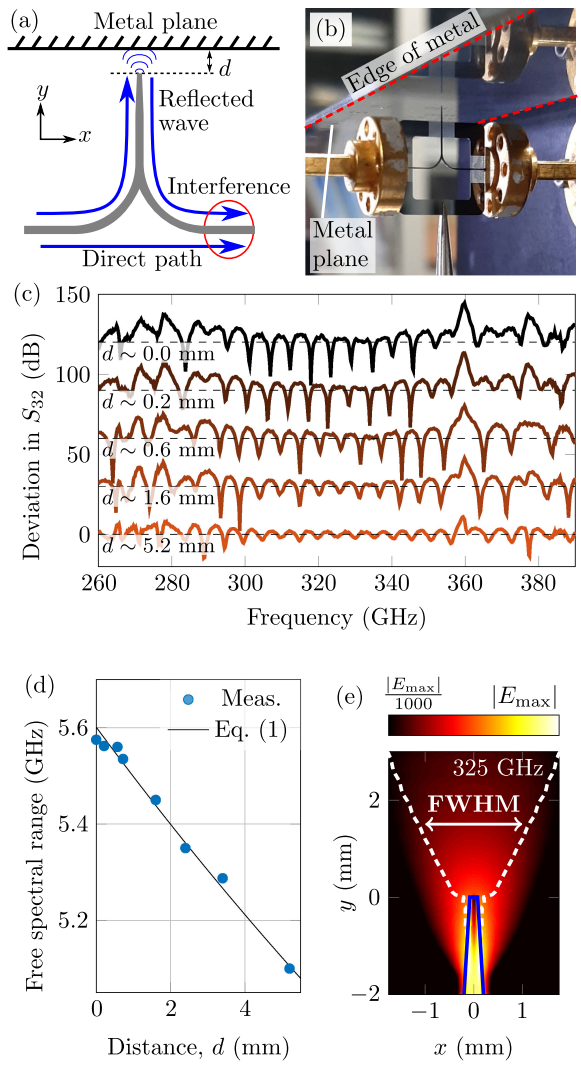

Fig. 4. Demonstration of terahertz sensing using the Y-junction, showing (a) illustration and (b) photograph of the sensing experiment, (c) deviation in S_{32} due to the influence of the metal, as normalized by the case in which the metal plane is removed, where individual traces that correspond to distinct values of distance, d, are separated from adjacent traces by 30 dB for clarity, (d) influence of distance d upon the spacing between fringes observed in (c), where the distance d is estimated from photographs by comparison with the known length of the spike that serves as a near-field probe, and (e) logarithmically scaled field magnitude plot of the dielectric rod that serves as a near-field probe structure, at 325 GHz.

conclude that additional reflection is generated in the Y-junction itself. If lower reflection is required, then the geometry of the Y-junction itself may be optimized [29].

B. Demonstration of Terahertz Near-Field Sensing

Near-field sensing has been identified as an attractive prospective application of terahertz waves [30]. This is because a terahertz wavelength is short relative to mm-waves and microwaves, facilitating strong localization of a sensing area. Terahertz waves are also non-damaging, non-ionizing, and are capable of penetrating a variety of optically-opaque materials to a modest physical depth. Furthermore, many substances of interest exhibit discernible spectral signatures in the terahertz range. For these reasons, terahertz technologies are anticipated to find uses in industrial inspection, medical imaging [31], and pharmaceutical quality control.

A Y-junction is suitable for sensing applications as it has three ports; a source and detector can be attached to one port each, and the third port defines a sensing area or probe. In this case, an interferometric sensing experiment is devised, as illustrated in Fig. 4(a) and shown in the photograph in Fig. 4(b). The source and detector are coupled to Ports 2 and 3, respectively, and Port 1 is employed as a probe. A portion of the energy that is coupled to Port 2 from the terahertz source will travel through the stem of the Y-junction to Port 1, where it will be radiated by the coupling spike, which operates as a dielectric rod antenna [32]. Thereafter, a portion of back-scattered energy from the metal plane is received by the probing coupling spike at Port 1, and transferred to Port 3. This energy interferes with the direct transmission between Ports 2 and 3. It is noted that, whilst this direct transmission is small, the reflected signal is expected to be comparable. This is because it undergoes $|S_{12}| \times |S_{31}| \sim 7$ dB loss due to two instances of transit through the Y-junction, as

well as further losses due to radiation of terahertz waves that are not re-admitted into the sensing area. Thus, the impact of interference is expected to be clearly discernible.

A metal plane is selected as it is a simple test case. The objective of the experiment is to determine whether the presence of the metal plane exerts a discernible impact on measured S_{32}. In order to isolate this impact, the measured transmission with the metal plane in-place is normalized against the case with no metal (i.e. corresponding to Fig. 3). A range of distances, d, are tested in this way, and a selection of results is shown in Fig. 4(c). Owing to normalization by the no-sample case, the dip at 360 GHz that is observed in Fig. 3(e) translates to a peak, which shows that energy is indeed received from the metal plane. Importantly, interference fringes can be clearly seen in all cases, and the spacing and depth of these fringes varies with the specific value of d. This is consistent with expectation, and supports the assertion of the specific signal paths that are indicated in Fig. 4(a). The free spectral range (i.e. frequency-separation between interference fringes) is extracted in the frequency range from 297 GHz to 346 GHz, and is plotted as a function of distance, d, in Fig. 4(d). These results show monotonic dependence of free spectral range upon d, which can be modeled with,

$$\text{Free spectral range} = \frac{c}{\Delta L_0 + d}, \tag{1}$$

which computes the change in frequency required for the difference in path length to increase by a single wavelength, thereby causing the interference condition to return to its original state. The constant ΔL_0 corresponds to the case where $d = 0$, i.e. the difference in optical path length acquired within the microphotonic Y-junction device itself. In this case, the average value of $\Delta L_0 = 53.6$ mm is computed from all measured results. In this way, Equation 1 can be employed to calibrate the Y-junction as a contactless depth gauge.

Further insight into the sensor's performance is desired. The dynamic range of the sensor may be estimated as peak deviation in measured S_{32} due to the influence of the metal plane. This occurs at 318 GHz, in the case where $d \sim 0$, and the measured deviation is -27 dB. Lateral resolution is also of interest, and hence simulated field distributions are employed in order to inspect field localization in the vicinity of the sensing area. The electric field distribution is shown in Fig. 4(e), for the case in which there is no sample, at 325 GHz. This frequency in particular is chosen as it is in the center of the measurable bandwidth. The full-width at half-maximum (FWHM) power is extracted, and is 420 μm at the surface of the probe—less than half a free-space wavelength. The FWHM increases thereafter as the fields diverge due to diffraction, but it remains below 1 mm for distances less than 230 μm.

The demonstrated sensing technique is closely related to terahertz optical coherence tomography [33], which can be employed for 3D object-penetrating imaging. Typically, such systems employ bulky free-space optics such as dielectric lenses, parabolic reflector dishes, and planar beam splitters in order to separate a terahetz beam into two paths. Thereafter, one of the paths is impinged upon a sample under test, and the other on a reference such as a planar mirror. Both paths are then recombined and made to interfere prior to detection. Overall, systems of this sort are generally quite large. On the other hand, the Y-junction presented in this work monolithically integrates an interferometer, coupling structures for the source and detector, and as a near-field sensing area—with a total device footprint of 14 × 16 mm^2. As such, unclad microphotonics can be viewed as a pathway towards a highly compact alternative to terahertz-range optical coherence tomography systems.

IV. Evanescent Coupler

A. Design and Characterization

A 2 × 2 evanescent coupler is a fundamental photonic component composed of two waveguides that are brought into close proximity, such that they can exchange energy via evanescent fields. As with the Y-junction that is expounded in Section III-A, it is capable of both splitting and combining terahertz radiation, albeit with a crucial distinction. For dielectric waveguides of this sort, field confinement is weaker for lower frequencies, and hence a greater proportion of modal fields are evanescent. Thus, the effect of near-field coupling between adjacent waveguides is stronger for lower frequencies, and hence all energy may be transferred from one waveguide to another over a shorter distance. This is the basis of frequency differentiation in 2 × 2 evanescent couplers, which renders its scope of uses distinct to that of Y-junctions.

We implement an evanescent coupler in which a pair of waveguides is parallel for a coupling length of 600 μm, over which they are separated by 50 μm; both values being less than a free-space wavelength. The two waveguides are brought into proximity by four 45° circular bends of radius 1 mm. Analysis of the loss of a waveguide bend in isolation is presented in the Supporting Information that accompanies this article. The evanescent coupler is housed within a protective frame. The coupler is fabricated using DRIE, and the resultant structure is shown in Figs. 5(a),(b). The device is experimentally characterized by interfacing hollow metallic waveguides to the coupling spikes at the relevant ports, as shown in Fig. 5(c),(d). The detected power is normalized by that of a straight waveguide, in order to remove the impact of the input coupling structure at the attach-point of the frame, as well as the measurement system. The results of this procedure are shown in Fig. 5(e), where it can be seen that close agreement with simulation is attained. Points at which S-parameters are slightly greater than 0 dB are considered the result of imperfect alignment in the reference measurement. The response of the 2 × 2 evanescent coupler confirms that it is indeed capable of frequency differentiation; low frequencies are more-readily transferred across the junction, with a peak in the vicinity of ∼290 GHz, and progressively less power is transferred as frequency is increased. The crossover point between these two modes of operation is situated at 320 GHz. It is also noted that, below ∼290 GHz, energy is progressively transferred back into the original waveguide after it is coupled across the junction, and hence S_{31} begins to fall as S_{21} recovers.

Port 4 is not intended to convey useful terahertz power, but rather, it accounts for undesired signals that are routed from Port 1 through reflection or stray evanescent coupling. Thus, A

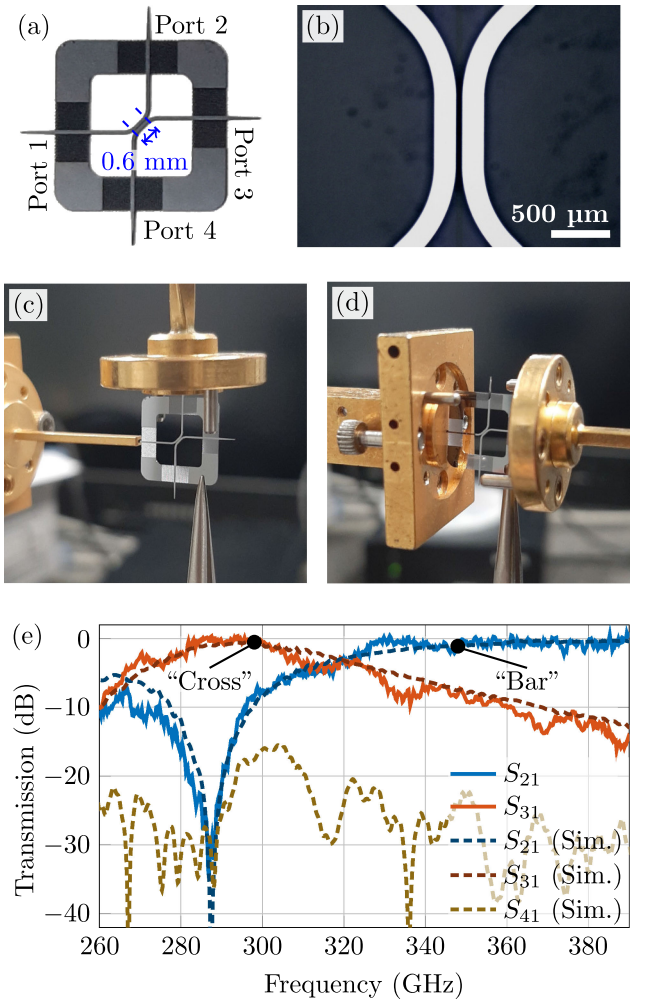

Fig. 5. A 2 × 2 evanescent coupler, showing (a) an annotated photograph and (b) a micrograph of the device, (c),(d) experimental characterization of S_{21} and S_{31}, respectively, and (e) measured and simulated S-parameters, indicating the carrier frequencies employed for the "Bar" and "Cross" channels in the communications demonstration in Section IV-B.

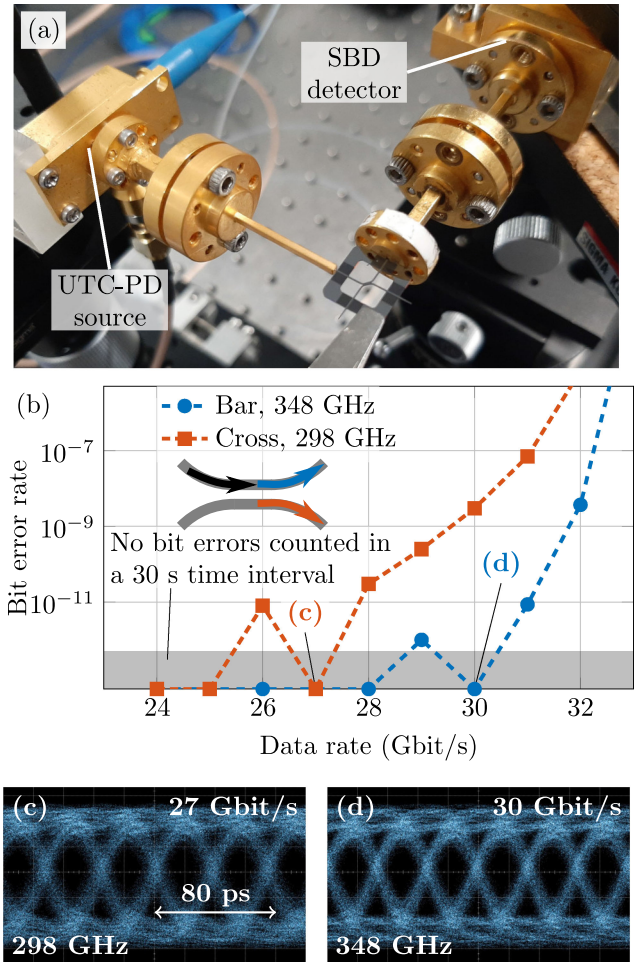

Fig. 6. Demonstration of two-channel terahertz communications using the 2 × 2 evanescent coupler, showing (a) a photograph of the experiment, in which the higher-frequency ("Bar") channel is being utilized, (b) measured bit error rates as a function of intended data rates, where points in the grey region correspond to zero counted bit-errors in a 30-second time interval, and (c),(d) selected eye diagrams from the low and high-frequency channels, respectively.

coupling spike is attached to this port in order to allow this waste power to radiate to free-space. For this reason, it is not deemed necessary to experimentally probe S_{41}. Simulation results given in Fig. 5(e) show that S_{41} accounts for less than −15 dB of stimulated power across the measurable bandwidth. In addition to this, the reflection response of the 2 × 2 coupler is included in the Supporting Information, and is found to be less than −10 dB across the measurable bandwidth.

B. Channelization for Terahertz Communications

The terahertz range is a portion of the electromagnetic spectrum with significant raw spectral bandwidth that is presently unoccupied by wireless services. Thus, terahertz waves have been identified as holding potential for high-volume wireless communications applications [34], [35]. Frequency-domain channelization at the physical level, in which signals of different carrier frequencies originate at distinct locations in a transceiver device, will be useful to support such applications. This is because independent terahertz sources can be dedicated to each channel, thereby increasing the overall transmit power of a given aggregate link, and extending range. It will also reduce the required complexity of intermediate-frequency and baseband circuits, by lowering the data rate that the individual circuit must process. That said, this comes at the cost of duplicating these circuits.

The frequency differentiation that is observed in Fig. 5(e) can serve as a simple form of terahertz-range frequency-domain channelization, and hence the evanescent coupler can operate as a frequency diplexer. Specifically, Ports 2 and 3 provide pathways for high, and low-frequency signals, respectively, to interface with Port 1. This forms two channels; the higher-frequency channel interfaces with Port 2, and is termed "Bar," and the lower-frequency channel at Port 3 is termed "Cross." Using the experimental setup that is shown in Fig. 6(a), We demonstrate that both channels are capable of supporting a terahertz signal that is modulated with digital information. This signal is generated optoelectronically, by down-conversion of

infrared-range power. To achieve this, a DC-biased uni-traveling carrier photo-diode (UTC-PD) is excited with two-color optical laser excitation, where the beat frequency corresponds to the desired output terahertz frequency. This is converted to terahertz power via a nonlinear process of optical rectification. The laser signal is modulated using non-return-to-zero on-off keying with a pseudo-random binary sequence, and the subsequent terahertz wave inherits this modulation. The modulated terahertz signal is output via a hollow metallic waveguide that is connected to Port 1 of the evanescent coupler. A Schottky barrier diode (SBD)-based detector employs direct detection to extract the modulating signal, which is then amplified using a low-noise amplifier with 29 dB gain and 38 GHz bandwidth, and subsequently clipped with a 45 Gbit/s limiting amplifier. This facilitates computation of the bit-error rate, and extraction of demodulated eye diagrams. The SBD is coupled to either Port 2 or 3 of the evanescent coupler, depending on which channel is presently being employed.

In this experiment, the Bar-channel employs a carrier frequency of 348 GHz, and the Cross-channel uses 298 GHz. These frequencies are selected in light of the raw spectral bandwidth available to each channel, as well as the output power of the UTC-PD, which is at maximum in the vicinity of 320 GHz to 330 GHz. For both channels, bit-error rate is measured as a function of data rate, and the results are shown in Fig. 6(b), where a grey region represents zero bit-errors in the time interval of the measurement. It can be seen that data rates of several tens of Gbit/s can be supported by both channels. From inspection of Fig. 5(e), each channel exhibits $\sim$40 GHz of available raw spectral bandwidth, which translates to an expected maximum data rate of $\sim$28 Gbit/s using non-return-to-zero on-off keying. The observed maximum error-free data rates correspond closely to this value, which is an indication that the waveguides, bend structures, and evanescent coupler are all of low dispersion. It is noted that our available measurement apparatus cannot acquire phase information, and hence it is not possible to probe dispersion directly. Eye diagrams of interest are shown in Figs. 6(c) and (d), where it can be seen that the "eye" is clearly open. The bit-error rate is, somewhat counter-intuitively, slightly higher for 26 Gbit/s than for 27 Gbit/s, for the low-frequency channel. Likewise, the bit-error rate is higher for 29 Gbit/s than for 30 Gbit/s in the case of the high-frequency channel. This may be due to statistical randomness in two experiments with a comparable absolute probability of bit-error. An alternative explanation is that key spectral features of the modulated signal at the lower data rate correspond to the location of narrowband reductions in transmission magnitude for the relevant channel.

It is noted that the channels are probed one-at-a-time to demonstrate terahertz communications, and hence this experiment innately neglects the possibility of cross-talk, which can negatively impact channel quality and achievable data rate. Indeed, the broadband direct-detection demodulation technique that is performed using a terahertz SBD is particularly susceptible to cross-talk. Nevertheless, this experiment shows that the 2×2 evanescent coupler can serve as a core component of frequency differentiation that is amenable to communications applications. In the future, all-silicon photonic filters [36] may be integrated directly with the evanescent coupler, and housed within the same supporting frame, in order to improve the out-of-band rejection of each channel. Coherent downconversion using a terahertz mixer and local oscillator source may also be useful to this end, as undesired signals may be removed with filters at the IF stage. However, such steps would constitute the development of a terahertz transceiver, and are therefore beyond the scope of this study, which is solely concerned with the unclad microphotonic platform and the core passive photonic devices that it can support.

V. Conclusion

We have presented a practical and versatile means to realize micro-scale silicon waveguides that are both substrateless and unclad, for the manipulation of terahertz waves. These waveguides are physically robust due to the frame structure, as well as broadband and highly efficient. Elementary photonic components have been developed for this platform, and their usefulness in practical terahertz-range applications has been demonstrated.

There is significant freedom in terms of the length and width of waveguides that remain structurally viable. As such, numerous diverse passive photonic components may be housed within a single supporting structure, and fabricated together, thereby realizing a sophisticated, monolithically-integrated terahertz passive circuit from a single photolithographic mask. Near-field contactless out-of-plane vertical coupling techniques [37] may allow a terahertz system to be constructed in a stacked, layer-wise manner, thereby enhancing integration density. It is also possible to integrate all-silicon antennas [32], [38], [39] in the same way, to provide wireless interfaces between independent terahertz systems.

Although a platform composed entirely of intrinsic silicon is restricted to passive devices only, hybrid integration with active terahertz integrated circuits provides an avenue to incorporate necessary components such as sources and detectors [40], as well as mixers [41], toward complete systems. Finally, although all demonstrations in the present study were restricted to the 300-GHz band, substrateless all-silicon photonic crystal waveguides have previously been scaled to 1 THz [42], and hence it is highly likely that unclad microphotonic devices are similarly scalable. For these reasons, this is a promising candidate to serve as a general-purpose integration platform for future compact terahertz systems.

References

[1] J. Hesler, A. Kerr, W. Grammer, and E. Wollack, "Recommendations for waveguide interfaces to 1 THz," in *Proc. ISSTT*, 2007, pp. 100–103.
[2] T. W. Crowe, B. Foley, S. Durant, K. Hui, Y. Duan, and J. L. Hesler, "VNA frequency extenders to 1.1 THz," in *Proc. IRMMW-THz*, 2011, doi: 10.1109/irmmw-THz.2011.6105028.
[3] A. von Bieren, E. De Rijk, J.-P. Ansermet, and A. Macor, "Monolithic metal-coated plastic components for mm-wave applications," in *Proc. IRMMW-THz*, 2014, doi: 10.1109/IRMMW-THz.2014.6956222.
[4] W. Otter *et al.*, "3D printed 1.1 THz waveguides," *Electron. Lett.*, vol. 53, no. 7, pp. 471–473, 2017.
[5] V. M. Lubecke, K. Mizuno, and G. M. Rebeiz, "Micromachining for terahertz applications," *IEEE Trans. Microw. Theory Tech.*, vol. 46, no. 11, pp. 1821–1831, Nov. 1998.

[6] T. Reck *et al.*, "Array technology for terahertz imaging," in *Passive and Active Millimeter-Wave Imaging XV*, vol. 8362. Bellingham, WA, USA: SPIE, 2012.
[7] T. J. Reck, C. Jung-Kubiak, J. Gill, and G. Chattopadhyay, "Measurement of silicon micromachined waveguide components at 500–750 GHz," *IEEE Trans. Terahertz Sci. Tech.*, vol. 4, no. 1, pp. 33–38, Jan. 2013.
[8] M. Alonso-del Pino, C. Jung-Kubiak, T. Reck, C. Lee, and G. Chattopadhyay, "Micromachining for advanced terahertz: Interconnects and packaging techniques at terahertz frequencies," *IEEE Microw. Mag.*, vol. 21, no. 1, pp. 18–34, Jan. 2020.
[9] P. Drude, "Zur elektronentheorie der metalle," *Annalen der physik*, vol. 306, no. 3, pp. 566–613, 1900.
[10] H.-T. Zhu, Q. Xue, J.-N. Hui, and S. W. Pang, "Design, fabrication, and measurement of the low-loss SOI-based dielectric microstrip line and its components," *IEEE Trans. Terahertz Sci. Technol.*, vol. 6, no. 5, pp. 696–705, Sep. 2016.
[11] H. Amarloo, N. Ranjkesh, and S. A. Safavi-Naeini, "Terahertz silicon–BCB–quartz dielectric waveguide: An efficient platform for compact THz systems," *IEEE Trans. Terahertz Sci. Technol.*, vol. 8, no. 2, pp. 201–208, Mar. 2018.
[12] N. Ranjkesh, M. Basha, A. Taeb, and S. Safavi-Naeini, "Silicon-on-glass dielectric waveguide–Part II: For THz applications," *IEEE Trans. Terahertz Sci. Technol.*, vol. 5, no. 2, pp. 280–287, Mar. 2015.
[13] H. Amarloo and S. Safavi-Naeini, ''," *IEEE Trans. Terahertz Sci. Technol.*, vol. 7, no. 4, pp. 433–439, Mar. 2017.
[14] N. Ranjkesh, S. Gigoyan, H. Amarloo, M. Basha, and S. Safavi-Naeini, "Broadband single-mode THz suspended silicon-on-glass waveguide," *IEEE Microw. Wireless Compon. Lett.*, vol. 28, no. 3, pp. 185–187, Mar. 2018.
[15] C. M. Yee and M. S. Sherwin, "High-Q terahertz microcavities in silicon photonic crystal slabs," *Appl. Phys. Lett.*, vol. 94, no. 15, 2009, Art. no. 154104.
[16] W. J. Otter, S. M. Hanham, N. M. Ridler, G. Marino, N. Klein, and S. Lucyszyn, "100 GHz ultra-high Q-factor photonic crystal resonators," *Sensors Actuators A Phys.*, vol. 217, pp. 151–159, 2014.
[17] K. Tsuruda, M. Fujita, and T. Nagatsuma, "Extremely low-loss terahertz waveguide based on silicon photonic-crystal slab," *Opt. Express*, vol. 23, no. 25, pp. 31 977–31 990, 2015.
[18] S. Hanham, C. Watts, W. Otter, S. Lucyszyn, and N. Klein, "Dielectric measurements of nanoliter liquids with a photonic crystal resonator at terahertz frequencies," *Appl. Phys. Lett.*, vol. 107, no. 3, 2015, Art. no. 032903.
[19] X. Yu, M. Sugeta, Y. Yamagami, M. Fujita, and T. Nagatsuma, "Simultaneous low-loss and low-dispersion in a photonic-crystal waveguide for terahertz communications," *Appl. Phys. Express*, vol. 12, no. 1, 2019, Art. no. 012005.
[20] D. Headland, M. Fujita, and T. Nagatsuma, "Bragg-mirror suppression for enhanced bandwidth in terahertz photonic crystal waveguides," *IEEE J. Sel. Top. Quantum Electron.*, vol. 26, no. 2, Mar./Apr. 2020, Art. no. 4900109.
[21] Y. Yang *et al.*, "Terahertz topological photonics for on-chip communication," *Nature Photon.*, vol. 14, pp. 446–451, 2020.
[22] W. Gao, X. Yu, M. Fujita, T. Nagatsuma, C. Fumeaux, and W. Withayachumnankul, "Effective-medium-cladded dielectric waveguides for terahertz waves," *Opt. Express*, vol. 27, no. 26, pp. 38 721–38 734, 2019.
[23] A. Malekabadi, S. A. Charlebois, D. Deslandes, and F. Boone, "High-resistivity silicon dielectric ribbon waveguide for single-mode low-loss propagation at F/G-bands," *IEEE Trans. Terahertz Sci. Technol.*, vol. 4, no. 4, pp. 447–453, Jul. 2014.
[24] S. M. Hanham, M. M. Ahmad, S. Lucyszyn, and N. Klein, "LED-switchable high-Q packaged THz microbeam resonators," *IEEE Trans. Terahertz Sci. Technol.*, vol. 7, no. 2, pp. 199–208, Mar. 2017.
[25] E. Akiki *et al.*, "A suspended silicon terahertz platform with low loss waveguide and high Q photonic crystal cavities," in *Proc. IRMMW-THz*, 2019, doi: 10.1109/IRMMW-THz.2019.8873957.
[26] W. J. Westerveld, S. M. Leinders, K. W. van Dongen, H. P. Urbach, and M. Yousefi, "Extension of Marcatili's analytical approach for rectangular silicon optical waveguides," *J. Lightw. Technol.*, vol. 30, no. 14, pp. 2388–2401, 2012.
[27] M. J. Adams, *An Introduction to Optical Waveguides*. Hoboken, NJ, USA: Wiley, 1981.
[28] P. H. Eilers, "A perfect smoother," *Analytical Chem.*, vol. 75, no. 14, pp. 3631–3636, 2003.
[29] Y. Zhang *et al.*, "A compact and low loss Y-junction for submicron silicon waveguide," *Opt. Express*, vol. 21, no. 1, pp. 1310–1316, 2013.
[30] M. Tonouchi, "Cutting-edge terahertz technology," *Nature Photon.*, vol. 1, no. 2, pp. 97–105, 2007.
[31] C. Yu, S. Fan, Y. Sun, and E. Pickwell-MacPherson, "The potential of terahertz imaging for cancer diagnosis: A review of investigations to date," *Quantative Imag. Med. Surgery*, vol. 2, no. 1, pp. 33–45, 2012.
[32] W. Withayachumnankul, R. Yamada, M. Fujita, and T. Nagatsuma, "All-dielectric rod antenna array for terahertz communications," *APL Photon.*, vol. 3, no. 5, 2018, Art. no. 051707.
[33] T. Nagatsuma, H. Nishii, and T. Ikeo, "Terahertz imaging based on optical coherence tomography," *Photon. Res.*, vol. 2, no. 4, pp. B64–B69, 2014.
[34] H.-J. Song and T. Nagatsuma, "Present and future of terahertz communications," *IEEE Trans. Terahertz Sci. Technol.*, vol. 1, no. 1, pp. 256–263, Sep. 2011.
[35] T. Nagatsuma, G. Ducournau, and C. C. Renaud, "Advances in terahertz communications accelerated by photonics," *Nature Photon.*, vol. 10, no. 6, pp. 371–379, 2016.
[36] A. Baldycheva, V. A. Tolmachev, T. S. Perova, Y. A. Zharova, E. V. Astrova, and K. Berwick, "Silicon photonic crystal filter with ultrawide passband characteristics," *Opt. Lett.*, vol. 36, no. 10, pp. 1854–1856, 2011.
[37] D. Headland, X. Yu, M. Fujita, and T. Nagatsuma, "Near-field out-of-plane coupling between terahertz photonic crystal waveguides," *Optica*, vol. 6, no. 8, pp. 1002–1011, 2019.
[38] W. Withayachumnankul, R. Yamada, C. Fumeaux, M. Fujita, and T. Nagatsuma, "All-dielectric integration of dielectric resonator antenna and photonic crystal waveguide," *Opt. Express*, vol. 25, no. 13, pp. 14 706–14 714, 2017.
[39] D. Headland, W. Withayachumnankul, R. Yamada, M. Fujita, and T. Nagatsuma, "Terahertz multi-beam antenna using photonic crystal waveguide and Luneburg lens," *APL Photon.*, vol. 3, no. 12, 2018, Art. no. 126105.
[40] X. Yu, J.-Y. Kim, M. Fujita, and T. Nagatsuma, "Efficient mode converter to deep-subwavelength region with photonic-crystal waveguide platform for terahertz applications," *Opt. Express*, vol. 27, no. 20, pp. 28 707–28 721, 2019.
[41] X. Yu, T. Ohira, J.-Y. Kim, M. Fujita, and T. Nagatsuma, "Waveguide-input resonant tunnelling diode mixer for terahertz communications," *Electron. Lett.*, vol. 56, no. 7, pp. 342–344, 2020.
[42] M. Sugeta, M. Fujita, and T. Nagatsuma, "Design and characterization of 1 THz-band photonic-crystal waveguides," in *Proc. JSAP Autumn Meeting*, 2018, Art. no. 20p-212A-15.

Daniel Headland received the Ph.D. degree from The University of Adelaide, Adelaide SA, Australia, in 2017. His thesis, which was titled "Efficient terahertz-range micro-beam control using flat optics," was awarded the Doctoral Research Medal and a Dean's Certificate of Doctoral Thesis Excellence. Thereafter, he completed a short-term Postdoctoral Fellowship at The University of Wuppertal, Germany, where he sought to expand the functionality of advanced terahertz-range CMOS circuits using classical optics techniques. He is currently with Osaka University, Toyonaka, Japan, where his research activities pertain primarily to terahertz photonics using intrinsic silicon, with a focus on waveguides, multiplexers, and antennas to support high-capacity communications applications.

Withawat Withayachumnankul (Senior Member, IEEE) received the bachelor's and master's degrees in electronic engineering from the King Mongkut's Institute of Technology Ladkrabang, Bangkok, Thailand, in 2001 and 2003, respectively, and the doctoral degree in electrical engineering with a special commendation from the University of Adelaide, Adelaide SA, Australia, in 2010. In 2015, he was a Research Fellow at the Japan Society for the Promotion of Science, Tokyo Institute of Technology, Tokyo, Japan. He has been a Visiting Researcher with Osaka University in recent years. He is currently an Associate Professor and the Postgraduate Coordinator with the University of Adelaide, and the Founding Leader of the Terahertz Engineering Laboratory. He has authored or coauthored more than 80 journal publications and has supervised six Ph.D. students to completion, all with commendation. His research interests include terahertz waveguides, antennas, radar, communications, and metrology. In 2010, he was awarded a 3-year Australian Research Council (ARC) Australian Postdoctoral Fellowship. He was the recipient of the IRMMW-THz Society Young Scientist Award in 2020. From 2017 to 2018, he was the Chair of the IEEE South Australia Joint Chapter on Microwave Theory and Techniques & Antennas and Propagation. In recent years, he has also been a Lead Investigator for three ARC grants, totaling to over AUD 1 M. He currently serves as an Associate Editor for the IEEE TRANSACTIONS ON TERAHERTZ SCIENCE AND TECHNOLOGY.

Xiongbin Yu received the B.E. degree from the Nagoya Institute of Technology, Nagoya, Japan, in 2017 and the Ph.D. degree from Osaka University, Toyonaka, Japan, in 2020. His thesis was titled "Terahertz Integrated Circuits Based on Photonic-crystal Waveguide Platform." Since 2020, he has been a specially appointed Assistant Professor with the Laboratory for Future Interdisciplinary Research of Science and Technology (FIRST), Tokyo Institute of Technology, Tokyo, Japan. Currently, he is involved in high-frequency electronic devices for terahertz communications applications. He received various awards during his doctoral program, including the Best Student Award from the 4th International Symposium on Microwave/Terahertz Science and Applications and the 8th International Symposium on Terahertz Nanoscience (2017), the Best Student Paper Award from the 40th International Progress in Electromagnetics Research Symposium (2018), the Student Prize from the 30th International Asia-Pacific Microwave Conference (2018), and the Best Oral Presentation from the 41th International Symposium on Optical Communications (2018).

Masayuki Fujita (Member, IEEE) received the Ph.D. degree from Yokohama National University, Yokohama, Japan, on ultrasmall and ultralow-threshold microdisk lasers. Subsequently, he joined Kyoto University and initiated research on photonic crystals. Next, he moved to Osaka University and was appointed the Research Director of the strategic basic research program CREST, "development of terahertz integrated technology platform through fusion of resonant tunneling diodes and photonic crystals" of the Japan Science and Technology Agency. He is currently an Associate Professor with the Graduate School of Engineering Science, Osaka University, Toyonaka, Japan. His research interests include terahertz materials and devices, photonic nanostructures and microstructures, and their applications. He currently serves as an Editor for Applied Physics Express, and a chair of the Technical Group on Terahertz Application Systems of Information and Communication Engineers (IEICE), Japan.

Tadao Nagatsuma (Fellow, IEEE) received the B.S., M.S., and Ph.D. degrees in electronic engineering from Kyushu University, Fukuoka, Japan, in 1981, 1983, and 1986, respectively. From 1986 to 2007, he was at the Nippon Telegraph and Telephone Corporation (NTT), Atsugi, Kanagawa, Japan. Since 2007, he has been with Osaka University, Toyonaka, Japan, where he is currently a Professor with the Graduate School of Engineering Science. His research interests include millimeter-wave and terahertz photonics and their applications to wireless communications, sensing, and measurement. He is a fellow of the Institute of Electronics, Information and Communication Engineers (IEICE), Japan and the Electromagnetics Academy. He currently serves as an Associate Editor for the IEEE PHOTONICS TECHNOLOGY LETTERS and the IEEE TRANSACTIONS ON TERAHERTZ SCIENCE AND TECHNOLOGY, and a Vice President of the IEICE and the Terahertz Systems Consortium.